



## Research Article

# Permanent Deformation and Temperature Monitoring of Subgrades Using Fiber Bragg Grating Sensing Technology

Youkun Cheng <sup>1,2</sup> and Zhenwu Shi <sup>1</sup>

<sup>1</sup>School of Civil Engineering, Northeast Forestry University, Harbin 150040, China

<sup>2</sup>School of Civil Engineering and Architecture, Harbin University of Science and Technology, Harbin 150080, China

Correspondence should be addressed to Zhenwu Shi; shizhenwu@126.com

Received 30 March 2020; Revised 29 November 2020; Accepted 10 January 2021; Published 31 January 2021

Academic Editor: Chengkuo Lee

Copyright © 2021 Youkun Cheng and Zhenwu Shi. This is an open access article distributed under the Creative Commons Attribution License, which permits unrestricted use, distribution, and reproduction in any medium, provided the original work is properly cited.

The hidden nature of subgrades makes the effective monitoring of their deformation very difficult. This paper addresses this issue by proposing the use of fiber Bragg grating (FBG) sensing technology. Here, an FBG is encapsulated within a monitoring tube formed from a polyvinyl chloride tube, and one end of the monitoring tube is fixed perpendicular to a concrete column, forming a cantilever beam monitoring system. The deformation is assessed according to the theoretical relationship between the horizontal strain on the FBG embedded in the monitoring tube and the vertical displacement of the cantilever beam. Then, the relationship between the variation in the wavelength of light reflected by the encapsulated FBG and the temperature and horizontal strain is obtained on this basis by calibration experiments. The monitoring tubes are buried at a proscribed depth below the top surface of the subgrade, which facilitates the monitoring of the deformation and temperature of the subgrade at different stages of construction through the collection of FBG wavelength data during different periods, such as after embedding the monitoring tubes, the completion of the test road surface, and during the period of operation. The proposed technology is verified by employing the system to monitor the instantaneous maximum deformation and permanent deformation of a subgrade under dynamic loads. The monitoring results demonstrate that the instantaneous maximum deformation values of the subgrade at 0.25 m and 0.5 m below the surface are 695.40  $\mu\text{m}$  and 574.02  $\mu\text{m}$ , respectively, and the corresponding permanent deformation values are 53.00  $\mu\text{m}$  and 41.54  $\mu\text{m}$ , respectively. The FBG sensor system is thereby verified to provide a reliable method for conducting long-term continuous, accurate, and efficient subgrade deformation and temperature monitoring.

## 1. Introduction

There are many factors that affect road service life [1]. Excessive settlement of highway subgrades is one of the main causes of roadway degradation, which can lead to serious driving safety risks [2–4]. However, conventional subgrade deformation monitoring methods are typically unable to provide timely and accurate information regarding the occurrence of subgrade deformation [5–7]. Accordingly, the development of effective subgrade deformation monitoring and early warning methods is essential for the prevention and control of highway degradation [8].

Fiber Bragg grating (FBG) sensing technology has developed rapidly over the past years [9–11] and represents an excellent alternative to conventional subgrade deformation

monitoring methods owing to its many advantages such as corrosion resistance, electromagnetic interference resistance, good waterproof performance, and high measurement precision [12]. Here, an FBG sensor employs a periodic variation in the refractive index along a short length of an optical fiber to obtain an optical filter that reflects specific bandwidths of light in response to the transmission of broad-spectrum light through the optical fiber. The periodic variation in the refractive index of optical fibers can be either uniform or nonuniform [13], and because the refractive index varies along the length of an optical fiber, the specific bandwidth of light reflected by the FBG is sensitive to temperature and strain. This sensing technology has been applied gradually over recent years for conducting engineering health monitoring [14–16] and geotechnical engineering monitoring [17, 18].

The specific applications have also varied widely to include numerous settings such as roadways [19], bridges [20, 21], high-speed railways [22], tunnels [23], aeronautics and astronautics [24, 25], oil recovery [26], and mining [27].

The specific designs and applications of FBG sensing technology have been the subject of intense development in recent years. For example, Guo et al. [28] applied a surface-mounted FBG strain sensor to successfully monitor the magnitude of the strain and its variation in an expressway via duct due to vehicle load pressure. Kesavan et al. [29] proposed an FBG sensor application for measuring the interfacial strain of reinforced concrete beams strengthened with carbon fiber-reinforced polymer (CFRP). An experimental application verified that the FBG sensor array effectively identified the beginning and expansion of CFRP separation from the concrete surface. An FBG humidity sensor has also been designed to monitor the corrosion rate of concrete sewer walls [30]. The FBG sensor was verified to provide high durability, good time response, and stability over an extended period in the corrosive hydrogen sulfide gas environment with high humidity. Accordingly, the FBG sensor was shown to have broad application prospects in harsh environments. Both long-gauge FBG and point FBG strain sensors were developed for monitoring the static and dynamic loads of a concrete railway bridge [31]. Experimental results demonstrated that both sensors were able to provide accurate strain measurements. A new type of mechanical sensor employing an FBG was proposed, and the design was demonstrated to improve the accuracy of damage detection and localization for civil engineering structures by amplifying the strain applied to the FBG sensor by a factor of about 36 [32]. Dys-hlyuk et al. [33] presented the experimental application of an FBG-based measurement method based on optical time-domain reflectometry (OTDR) for monitoring strain in bent reinforced concrete beams. The proposed method was demonstrated to provide results that were consistent with those of direct spectral measurements. A vibration detection method based on FBG sensing technology was proposed to accurately measure the physical and mechanical properties of soil [34]. The data collected by the FBG sensor were demonstrated theoretically and experimentally to reflect vibration conditions clearly and quantitatively. Bellas and Voulgaridis [35] responded to the impact of geotechnical disasters on community housing by developing an advanced FBG-based method for monitoring the health of housing structures and serving as an early warning system. Nan et al. [36] contributed toward the prevention of subway tunnel collapse by applying ultraweak FBG sensing technology to detect the distributed vibrational response of the FBG positioned on the tunnel wall and the track bed, and the occurrence and characteristics of intrusion events simulated by the discrete and continuous pulses of an excavator were recognized under two loading attitudes. The above studies have demonstrated that FBG sensing technology can be implemented in a wide array of engineering applications under complex and harsh conditions. Accordingly, this technology has been applied for monitoring subgrade deformation [37, 38]. However, a sufficiently exact relationship between the specific bandwidth of light reflected by the

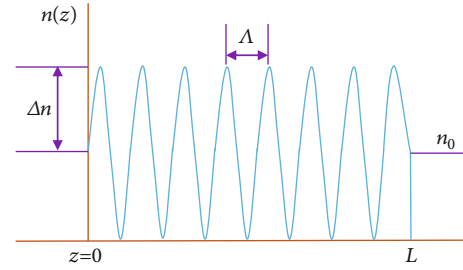


FIGURE 1: Refractive index distribution of fiber Bragg grating (FBG).

FBG and the vertical displacement of the subgrade was not established in these past studies, and the proposed methodology was unable to monitor subgrade temperature.

The present work addresses the shortcomings of past efforts seeking to apply FBG sensing technology toward subgrade deformation and temperature monitoring. Here, an FBG with a uniformly distributed variation in the index of refraction is encapsulated within a monitoring tube formed from a polyvinyl chloride (PVC) tube, and one end of the monitoring tube is fixed perpendicular to a concrete column, forming a cantilever beam monitoring system. The deformation is assessed according to the theoretical relationship between the horizontal strain on the FBG embedded in the monitoring tube and the vertical displacement of the cantilever beam. Then, the relationship between the variation in the wavelength of light reflected by the encapsulated FBG and the temperature and horizontal strain is obtained on this basis by calibration experiments. The monitoring tubes are buried at a proscribed depth below the top surface of the subgrade, which facilitates the monitoring of the deformation and temperature of the subgrade at different stages of construction through the collection of FBG wavelength data during different periods, such as after embedding the monitoring tubes, the completion of the test road surface, and during the period of operation. The proposed technology is verified by employing the system to monitor the instantaneous maximum deformation and permanent deformation of a subgrade under dynamic loads. The results verify that the deformation and temperature of the subgrade can be monitored in situ even after the completion of highway pavement construction, and each measurement can be completed in a few minutes.

## 2. Working Principles of FBG Sensors

*2.1. Transmission Principle.* The axial refractive index distribution of a uniform period FBG can be given as follows [39]:

$$n(z) = n_0 + \Delta n_{\max} \cdot \cos\left(\frac{2\pi}{\Lambda} z\right), \quad (1)$$

where  $n_0$  is the refractive index of the optical fiber core,  $\Delta n_{\max}$  is the maximum change in  $n_0$ ,  $\Lambda$  is the period length of the uniform grating, and  $z$  is the axial position along the optical fiber. The refractive index distribution is illustrated in Figure 1 [40].

According to coupled mode theory, the wavelengths of broad-spectrum light transmitted through an optical fiber

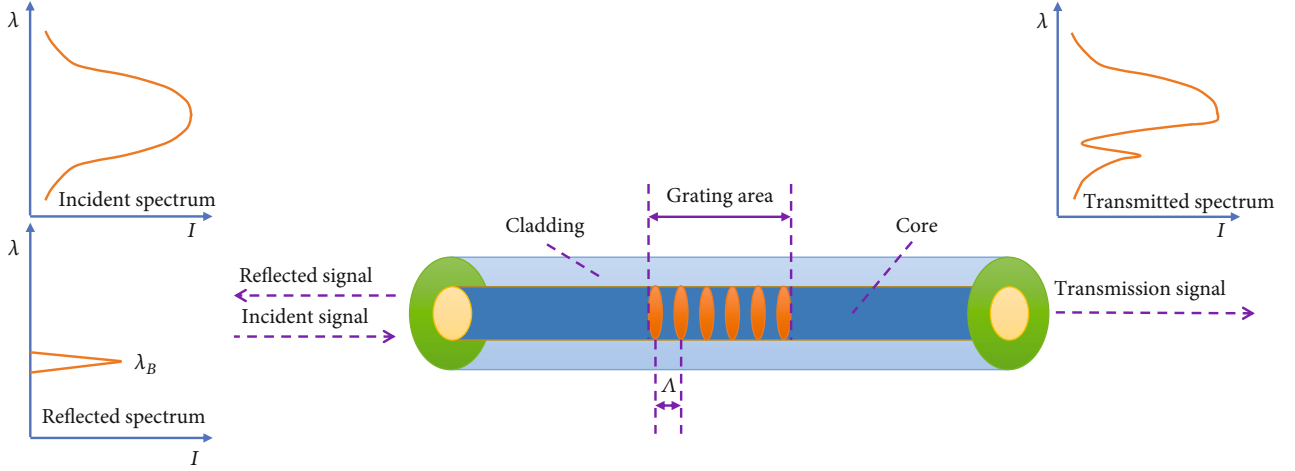


FIGURE 2: Schematic illustrating the spectral response of an FBG.

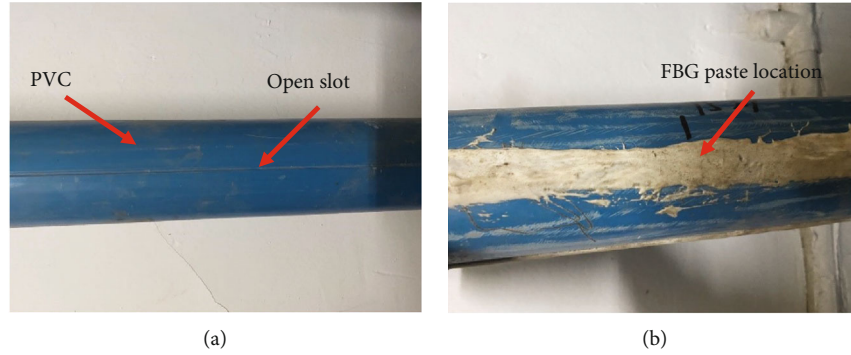


FIGURE 3: FBG packaging: (a) PVC tube slotting; (b) silicon rubber packaging.

that meet the Bragg wavelength condition of the FBG will be reflected back to the incident end of the optical fiber, and the light of all other wavelengths will pass through freely [41]. This condition is illustrated in Figure 2.

**2.2. Basic Sensing Principle.** Through coupling between the core mode of forward light transmission and the core mode of backward light transmission, the energy of the core mode of forward transmission is transferred to the core mode of backward transmission, forming the reflection of the incident wave [42]. The reflected wavelength of an FBG is given as follows:

$$\lambda_B = 2n_{\text{eff}}\Lambda, \quad (2)$$

where  $n_{\text{eff}}$  is the equivalent refractive index of the optical fiber core. The elasto-optic effect of the fiber itself causes the value of  $n_{\text{eff}}$  to change with changes in the strain state of the fiber, which changes the value of  $\lambda_B$  reflected from the FBG [43]. As such, the value of  $\lambda_B$  represents a measure of the strain state of the optical fiber.

TABLE 1: The technical parameters of FBGs.

| Item                 | Technical parameters        |
|----------------------|-----------------------------|
| Central wavelength   | 1510-1590 nm                |
| Wavelength tolerance | $\pm 0.3$ nm                |
| 3 dB bandwidth       | $\leq 0.3$ nm               |
| Reflectivity         | $\geq 90\%$                 |
| Isolation            | $\geq 15$ dB                |
| Fiber type           | SMF-28                      |
| Grating length       | Grating length $\leq 10$ mm |

If the influence of changes in the temperature is not taken into account, the change in  $\lambda_B$  owing to tensile and compressive axial strain  $\varepsilon$  on the FBG can be expressed as follows:

$$\Delta\lambda_B = \lambda_B(1 - P_e)\varepsilon, \quad (3)$$

where  $P_e$  is the effective photoelastic coefficient. Therefore, the axial strain can be calculated as follows:

$$\varepsilon = \frac{1}{(1 - P_e)} \left[ \frac{\Delta\lambda_B}{\lambda_B} \right]. \quad (4)$$

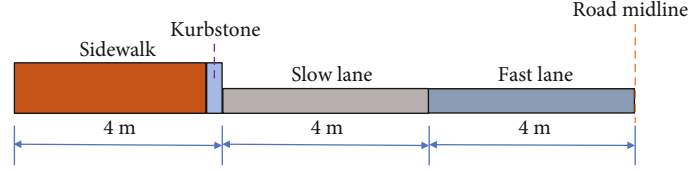


FIGURE 4: Layout of one half of a standard four-lane roadway.

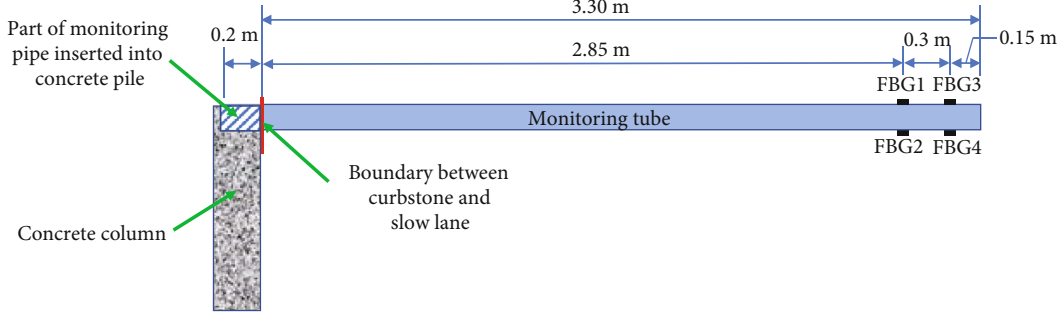


FIGURE 5: FBG cantilevered monitoring tube structure.

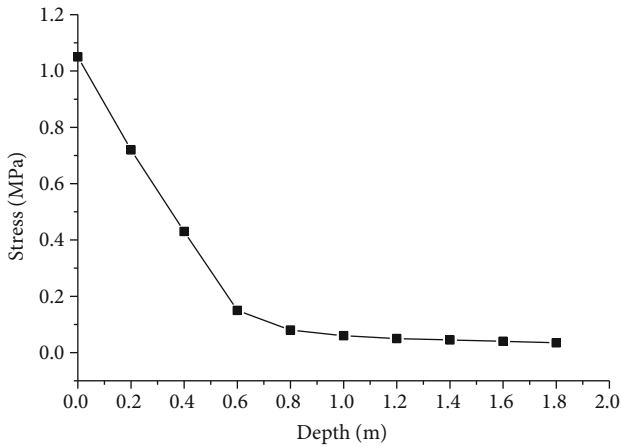


FIGURE 6: Vertical dynamic stress of a subgrade with respect to depth owing to vehicle loading [46].

When accounting for changes in the temperature, the thermo-optic effect and thermal expansion effect of FBG materials lead to a shift in  $\lambda_B$  owing to a change  $\Delta\Lambda$  in the value of  $\Lambda$  [43, 44]. From equation (2), the value of  $\Delta\lambda_B$  caused by a temperature change  $\Delta T$  can be expressed as follows:

$$\begin{aligned}\Delta\lambda_B &= 2\Delta n_{\text{eff}} \cdot \Lambda + 2n_{\text{eff}} \cdot \Delta\Lambda \\ &= 2 \left[ \frac{\partial n_{\text{eff}}}{\partial T} \Delta T + (\Delta n_{\text{eff}})_{\text{ep}} + \frac{\partial n_{\text{eff}}}{\partial r} \Delta r \right] \Lambda + 2n_{\text{eff}} \cdot \frac{\partial \Lambda}{\partial T} \Delta T.\end{aligned}\quad (5)$$

Here,  $\partial n_{\text{eff}}/\partial T$  is the refractive index temperature coefficient of the fiber grating;  $(\Delta n_{\text{eff}})_{\text{ep}}$  is the elasto-optic effect produced by the thermal expansion effect;  $\partial n_{\text{eff}}/\partial r$  is the

waveguide effect produced by the thermal expansion effect, where  $r$  is the diameter of the optical fiber; and  $\partial \Lambda/\partial T$  is the linear thermal expansion coefficient of the FBG. The right side of equation (5) can now be divided by the right side of equation (2) to obtain the following:

$$\frac{\Delta\lambda_B}{\lambda_B} = \left( \frac{\partial n_{\text{eff}}}{\partial T} \cdot \frac{1}{n_{\text{eff}}} + \frac{\Delta\Lambda}{\Delta T} \cdot \frac{1}{\Lambda} \right) \cdot \Delta T + \frac{1}{n_{\text{eff}}} \left[ (\Delta n_{\text{eff}})_{\text{ep}} + \frac{\partial n_{\text{eff}}}{\partial r} \cdot \Delta r \right], \quad (6)$$

where  $\partial n_{\text{eff}}/\partial T \cdot 1/n_{\text{eff}}$  is the thermo-optic coefficient of the FBG, which is expressed by  $\zeta$ ;  $\Delta\Lambda/\Delta T \cdot 1/\Lambda$  is the thermal expansion coefficient of the optical fiber, which is expressed by  $\alpha$ ; and  $1/n_{\text{eff}}[(\Delta n_{\text{eff}})_{\text{ep}} + \partial n_{\text{eff}}/\partial r \cdot \Delta r]$  is the comprehensive action coefficient of the elasto-optic and waveguide effects, which can be expressed by  $K_H$ . Accordingly, equation (6) can be arranged as follows:

$$\frac{\Delta\lambda_B}{\lambda_B} = (\zeta + \alpha) \cdot \Delta T + K_H, \quad (7)$$

which yields the following expression:

$$\Delta\lambda_B = [(\zeta + \alpha) \cdot \Delta T + K_H] \cdot \lambda_B. \quad (8)$$

However, the influence of the elasto-optic and waveguide effects caused by thermal expansion on the temperature sensitivity coefficient is very weak. Therefore,  $K_H$  can be ignored, and equation (8) can be simplified as

$$\Delta\lambda_B = (\zeta + \alpha) \cdot \Delta T \cdot \lambda_B. \quad (9)$$

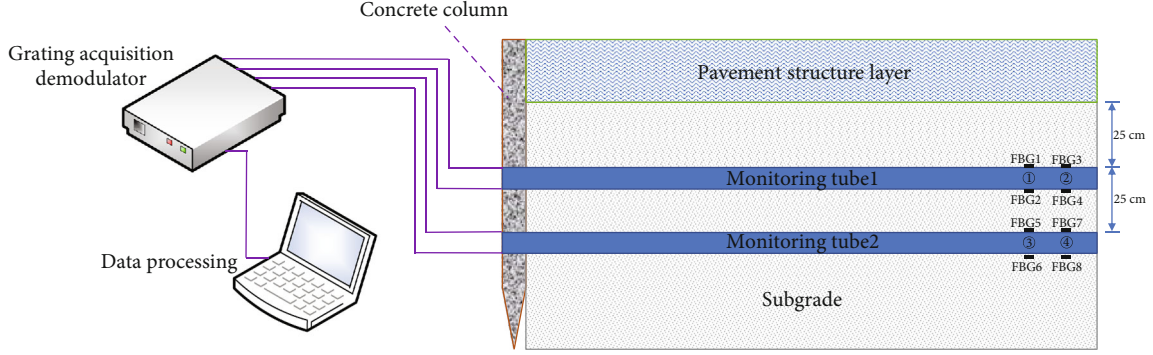


FIGURE 7: Cross-sectional layout plan of monitoring tubes.

We can then combine equations (3) and (9) to obtain the change in  $\lambda_B$  owing to both strain and temperature as follows:

$$\Delta\lambda_B = [(1 - P_e)\varepsilon + (\zeta + \alpha)\Delta T] \cdot \lambda_B. \quad (10)$$

This can be further simplified using the definitions  $(1 - P_e) \cdot \lambda_B = K_\varepsilon$  and  $(\zeta + \alpha) \cdot \lambda_B = K_T$ , as follows:

$$\Delta\lambda_B = K_\varepsilon \varepsilon + K_T \Delta T. \quad (11)$$

Here,  $K_\varepsilon$  is denoted as the strain sensitivity coefficient, and  $K_T$  is denoted as the temperature sensitivity coefficient.

### 3. Monitoring Tube Design and FBG Calibration

**3.1. FBG Monitoring Tube Design.** An FBG is fragile and vulnerable to damage, so it cannot be directly embedded in the subgrade. Therefore, an FBG must be packaged within a suitable carrier structure, which can then be embedded in the subgrade. The present work employs a circular PVC tube with a diameter of 10 cm as the FBG carrier. As shown in Figure 3(a), the PVC tube is first slotted in advance, and slotting is applied symmetrically to the other side of the tube as well. Then, a single FBG is fixed in the upper and lower slots of the PVC tube using 101 glue and then encased with NANDA 703 silicone rubber, as shown in Figure 3(b) for the upper FBG. The technical parameters of FBGs used in the paper are shown in Table 1.

Figure 4 presents a cross-sectional schematic of the traffic lanes of a standard roadway. Past studies have demonstrated that the maximum dynamic stress generated by vehicle loading appears directly under the wheels over a specific depth range of the subgrade [45]. Moreover, according to traffic rules and standard driving habits, the slow lane is mainly used by large and heavy vehicles, which travel down the middle of the slow lane under normal circumstances. Therefore, these positions in the slow lane represent the points of maximum subgrade deformation. Accordingly, the present work adopts the cantilever beam monitoring system illustrated in Figure 5. Here, the base end of the cantilever beam is embedded within a concrete column, and two FBGs are packaged symmetrically in the upper and lower slots at the end of the monitoring tubes.

TABLE 2: Center reflection wavelength  $\lambda_B$  of representative FBGs in the absence of strain at a temperature of 21.3°C.

| FBG number | Wavelength $\lambda_B$ (nm) | FBG number | Wavelength $\lambda_B$ (nm) |
|------------|-----------------------------|------------|-----------------------------|
| 1          | 1528.6743                   | 5          | 1549.9876                   |
| 2          | 1533.1821                   | 6          | 1554.6176                   |
| 3          | 1538.2894                   | 7          | 1559.1890                   |
| 4          | 1544.9197                   | 8          | 1563.0514                   |

The positioning of the FBGs is based on a standard heavy truck wheelbase width of 2 m with consideration for the contact area between the tire and the ground. The standard width of tire contact with the ground is approximately 0.3 m based on the heavy vehicle tire most commonly used, an axle load of 100 kN, and tire pressure of 0.7 MPa. Accordingly, the distance between the inner and outer FBGs and the base end of the cantilever beam is 2.85 m and 3.15 m, respectively, and the FBGs are arranged symmetrically at the upper and lower positions of the monitoring tube to realize simultaneous monitoring of subgrade deformation and temperature. As shown in Figure 5, the centers of FBG1 and FBG2 are on the same plumb line, and the centers of FBG3 and FBG4 are on the same plumb line. This represents an improved configuration relative to previously published work [46], where each monitoring tube was equipped with 8 FBG monitoring points typically. However, the monitoring points close to the base end of the cantilever provided limited information due to the fixed constraint at the base end. Therefore, the FBGs are placed only directly under the vehicle track in the present work.

**3.2. Monitoring Scheme Design.** As shown in Figure 6, past research has demonstrated that the vertical dynamic stress of a subgrade owing to automobile loading decreases linearly with increasing subgrade depth in the range of 0.0–0.6 m, and that the dynamic stress decreases much more slowly at depths greater than 0.6 m [47, 48]. This linearity is employed in the present work by adopting two FBG monitoring tubes buried at 0.25 m and 0.50 m below the top surface of the roadbed, as illustrated in Figure 7, which includes the optical fiber configuration employed in conjunction with an FBG acquisition demodulator and data processing module.

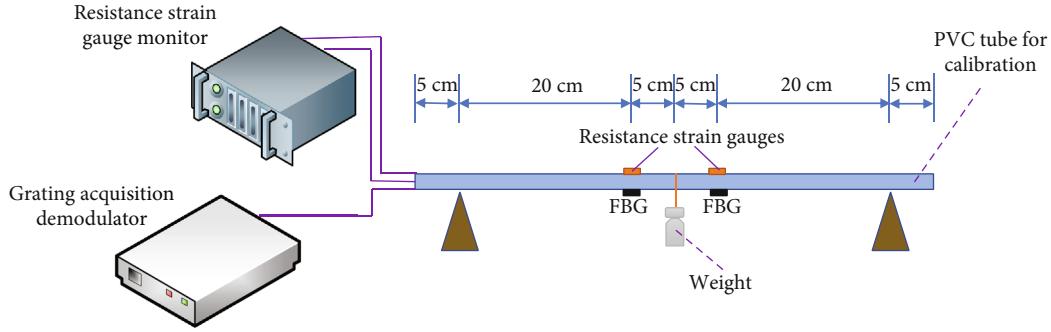


FIGURE 8: Layout of strain sensitivity coefficient calibration experiments.

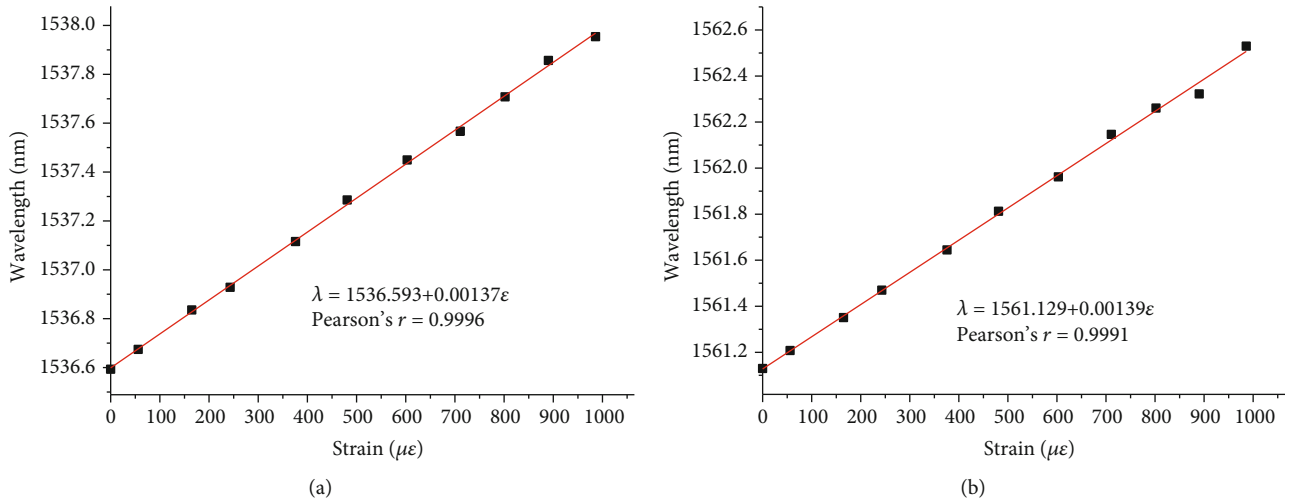


FIGURE 9: Calibration curves of the strain sensitivity coefficients  $K_\epsilon$ : (a) FBG with an initial  $\lambda_B$  value of 1536.593 nm; (b) FBG with an initial  $\lambda_B$  value of 1561.129 nm.

FC/APC connector was welded to one end of the optical fiber using a fiber fusion splicer, which would be connected to the interrogator when conducting tests. The monitoring system has 4 arrays of 2 FBG sensors each, as Figure 7 shows with the 4 lines coming out from the monitoring tubes.

**3.3. FBG Calibration.** Accurate monitoring of the subgrade deformation and temperature requires that we first calibrate the strain sensitivity coefficient  $K_\epsilon$  and temperature sensitivity coefficient  $K_T$  of the FBGs employed in the proposed monitoring system. However, we first obtained the values of  $\lambda_B$  for 8 representative FBGs installed within monitoring tubes in the absence of strain at a temperature of 21.3°C, and the results are listed in Table 2.

The monitoring tubes were so long that the FBGs on them were not easy to be calibrated after encapsulation, so 2 FBGs were selected for calibrating the strain sensitivity coefficient  $K_\epsilon$  and the temperature sensitivity  $K_T$  in the laboratory. According to the previous calibration experiment results, there is little difference between the  $P_e$ ,  $\zeta$ , and  $\alpha$  values of the same model FBGs from the same manufacturer, so it was assumed that the  $P_e$ ,  $\zeta$ , and  $\alpha$  values of the 8 FBGs used on the monitoring tubes are equal to those of the 2 FBGs used in the calibration experiment.

TABLE 3: Strain sensitivity coefficients  $K_\epsilon$  of representative FBGs.

| FBG number | Strain sensitivity coefficient (pm/ $\mu\epsilon$ ) | FBG number | Strain sensitivity coefficient (pm/ $\mu\epsilon$ ) |
|------------|---|------------|---|
| 1          | 1.36  | 5          | 1.38  |
| 2          | 1.37  | 6          | 1.39  |
| 3          | 1.37  | 7          | 1.39  |
| 4          | 1.38  | 8          | 1.39  |

**3.3.1. Calibration of Strain Sensitivity Coefficient.** Two FBGs were selected for calibrating the strain sensitivity coefficient  $K_\epsilon$  at a temperature of 21.3°C according to the experimental setup illustrated in Figure 8. Here, 60 cm sections of PVC monitoring tubes were applied, and FBGs were installed on the lower tube sides in an equivalent manner as described in Subsection 3.1. Center reflection wavelengths  $\lambda_B$  of 1536.593 nm and 1561.129 nm were first obtained for these two FBGs in the absence of strain. In addition, resistance strain gauges were pasted on the upper tube sides directly above the FBGs. The two ends of the PVC tube were fixed, and a variable weight was applied at the midpoint of the tube. Then, strain and  $\lambda_B$  data were collected simultaneously from the resistance strain gauge monitor and the grating

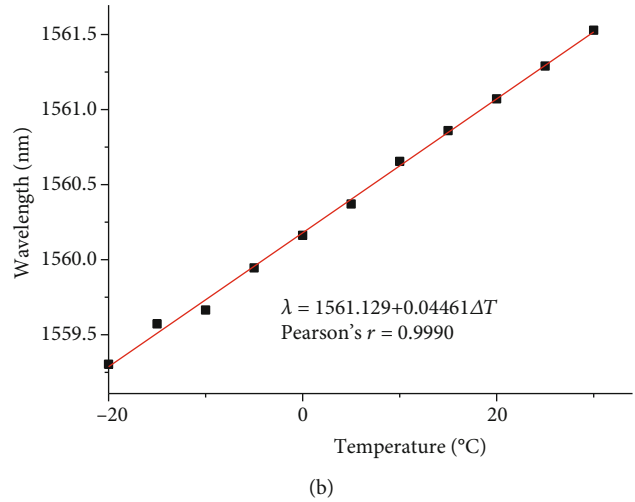
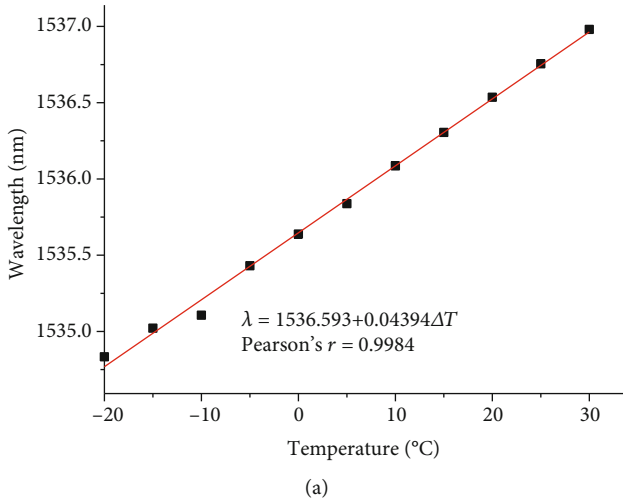


FIGURE 10: Calibration curves of temperature sensitivity coefficients  $K_T$ : (a) FBG with an initial  $\lambda_B$  value of 1536.593 nm; (b) FBG with an initial  $\lambda_B$  value of 1561.129 nm.

TABLE 4: Temperature sensitivity coefficients  $K_T$  of representative FBGs.

| FBG number | Temperature sensitivity coefficient (pm/°C) | FBG number | Temperature sensitivity coefficient (pm/°C) |
|------------|---|------------|---|
| 1          | 43.71                                       | 5          | 44.32                                       |
| 2          | 43.84                                       | 6          | 44.46                                       |
| 3          | 43.99                                       | 7          | 44.59                                       |
| 4          | 44.18                                       | 8          | 44.70                                       |

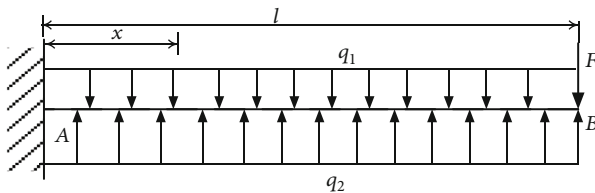


FIGURE 11: Stress analysis of the cantilevered monitoring tube structure.

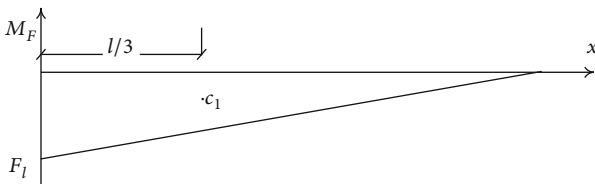


FIGURE 12: Schematic illustrating the bending moment of the cantilever beam under load  $F$ .

acquisition demodulator, respectively. The experimental resistance strain gauge setup provided an accuracy of  $1 \mu\epsilon$  and a measurement range of  $-19999 \mu\epsilon$  to  $+38000 \mu\epsilon$ . The relationships between  $\lambda_B$  and the measured strain are presented in Figure 9. The calibration results indicate that the

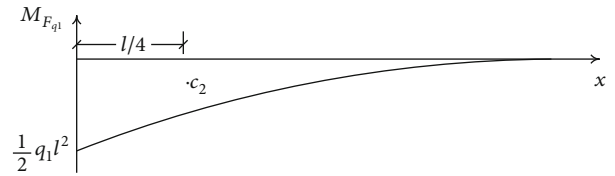


FIGURE 13: Schematic illustrating the bending moment of the cantilever beam under distributed load  $q_1$ .

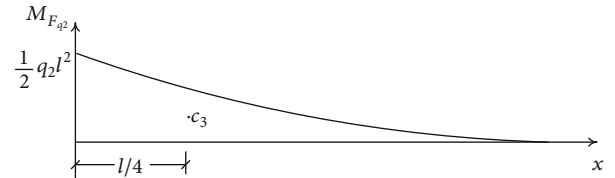


FIGURE 14: Schematic illustrating the bending moment of the cantilever beam under distributed load  $q_2$ .

values of  $\lambda_B$  for the FBGs change linearly with respect to strain over the investigated strain range, indicating that the FBGs respond uniformly over that range. The values of  $K_\epsilon$  were obtained for the two FBGs from the slopes of the lines fitted to the plotted data, which were  $1.37 \text{ pm}/\mu\epsilon$  and  $1.39 \text{ pm}/\mu\epsilon$ . According to the calibration results, the strain sensitivity coefficients  $K_\epsilon$  of the FBGs on the monitoring tube could be calculated by  $K_\epsilon = (1 - P_e) \cdot \lambda_B$ . The values of  $K_\epsilon$  obtained similarly for all 8 FBGs listed in Table 2 are listed in Table 3.

3.3.2. *Temperature Sensitivity Calibration.* The two FBGs employed for strain sensitivity coefficient calibration were again employed for temperature sensitivity calibration over an experimental temperature range of  $-20^\circ\text{C}$  to  $30^\circ\text{C}$ . A frequency conversion refrigerator was used to control the temperature between  $-20^\circ\text{C}$  and  $10^\circ\text{C}$ , and the temperature

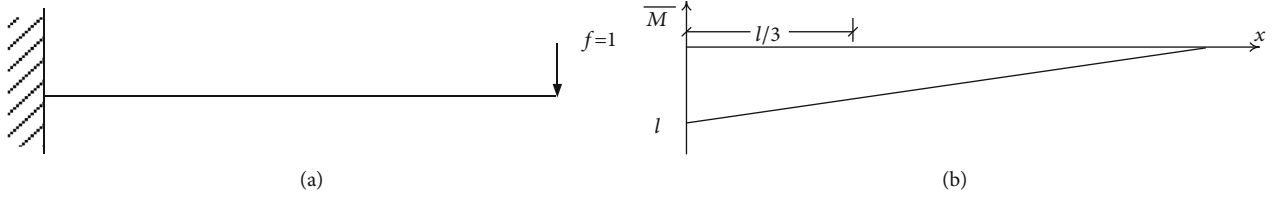


FIGURE 15: Load diagram (a) and bending moment diagram (b) under a unit force  $f$ .

inside the refrigerator was monitored using a K-type thermocouple connected with a tt-k-24-sle thermocouple line to a temperature monitor located outside of the refrigerator. Testing at temperatures in the range of  $10^{\circ}\text{C}$  to  $30^{\circ}\text{C}$  was conducted in a laboratory equipped with a constant frequency air conditioner, and the temperature was again monitored with a K-type thermocouple. The change in the values of  $\lambda_B$  for the FBGs with respect to temperature was monitored every  $5^{\circ}\text{C}$  in the absence of strain. The experimental results are shown in Figure 10. The temperature calibration results indicate that the values of  $\lambda_B$  for the FBGs change linearly with respect to the temperature over the investigated temperature range, indicating that the FBGs respond uniformly over that range. The values of  $K_T$  were obtained for the two FBGs from the slopes of the lines fitted to the plotted data, which were  $43.94 \text{ pm}/^{\circ}\text{C}$  and  $44.61 \text{ pm}/^{\circ}\text{C}$ . According to the calibration results, the temperature sensitivity coefficients  $K_T$  of the FBGs on the monitoring tube could be calculated by  $K_T = (\zeta + \alpha) \cdot \lambda_B$ . The values of  $K_T$  obtained similarly for all 8 FBGs listed in Table 2 are listed in Table 4.

#### 4. Principle of Deformation Calculation

As discussed above, the horizontal strain on a monitoring tube can be determined according to the change  $\Delta\lambda_B$  in the wavelength of the light reflected by the FBG. However, monitoring the deformation of the subgrade based on the cantilevered monitoring tubes illustrated in Figures 5 and 7 requires that the relationship between the horizontal strain and the vertical deflection of a monitoring tube be determined. This is evaluated according to the stress conditions acting on the axis of the cantilever beam, as illustrated in Figure 11. Here, the beam length between points A and B is  $l$ ,  $x$  is the horizontal distance from the fixed end to any position along the cantilever beam, and  $q_1$  and  $q_2$  are uniformly distributed loads, respectively, on the upper and lower surfaces of the beam owing to a force  $F$  applied at point B.

The conditions illustrated in Figure 11 are further analyzed by considering the bending moments under load  $F$  and distributed loads  $q_1$  and  $q_2$ . First, the moment equation of the cantilever beam under load  $F$  is given as

$$M(x) = -F(l - x), \quad (12)$$

according to the moment diagram shown in Figure 12, where  $c_1$  is the centroid of the bending moment diagram. The bending moments of the cantilever beam under  $q_1$  and  $q_2$  are, respectively, analyzed accordingly to the moment diagrams shown in Figures 13 and 14, where  $c_2$  and  $c_3$  are the respective

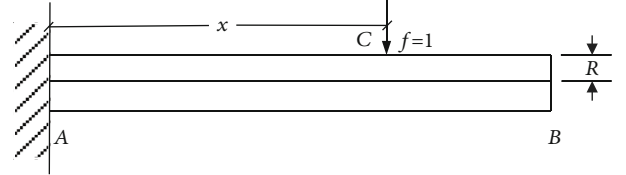


FIGURE 16: Load per unit force  $f$  at any point along the cantilever beam.

centroids of the two bending moment diagrams, and the bending moment equations are given as follows:

$$\begin{aligned} M_1(x) &= -\frac{q_1(l-x)^2}{2}, \\ M_2(x) &= \frac{q_2(l-x)^2}{2}. \end{aligned} \quad (13)$$

Accordingly, these bending moment diagrams represent quadratic parabolas.

Extending the above analysis, a unit force  $f$  is applied to the end of the cantilever beam, as shown in Figure 15(a), and the bending moment diagram is shown in Figure 15(b). Accordingly, the bending moment equation is given as follows:

$$\overline{M}(x) = -(l - x). \quad (14)$$

The ordinate values of the unit load bending moment diagram corresponding to the center of gravity of the bending moment of the cantilever under applied loads  $F$ ,  $q_1$ , and  $q_2$  are, respectively,

$$\begin{aligned} \overline{M}_{C1} &= \frac{2l}{3}, \\ \overline{M}_{C2} &= \frac{3l}{4}, \\ \overline{M}_{C3} &= \frac{3l}{4}. \end{aligned} \quad (15)$$

The vertical deformation of point B can be obtained using graph multiplication as follows:

$$\Delta B = \frac{1}{EI} \left( Fl \cdot l \cdot \frac{2l}{3} + \frac{1}{2} q_1 l^2 \cdot l \cdot \frac{l}{4} - \frac{1}{2} q_2 l^2 \cdot l \cdot \frac{l}{4} \right), \quad (16)$$



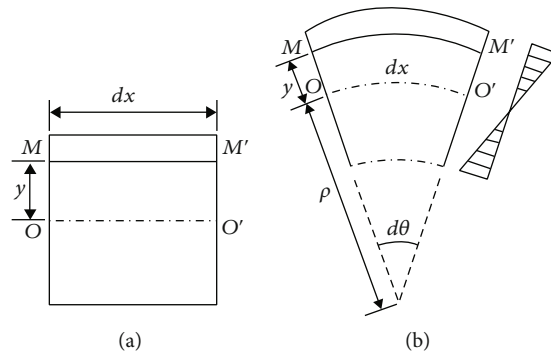


FIGURE 17: Bending strain diagrams: (a) unstressed diagram; (b) poststressed diagram.



FIGURE 18: Monitoring tube embedding process underneath a section of a test roadway: (a) trenching; (b) concrete column pouring for anchoring cantilevers; (c) laying of a monitoring tube.

TABLE 5: Initial center wavelengths of the reflected light from the FBGs and corresponding subgrade temperatures obtained immediately after laying the monitoring tubes.

| FBG number  | Wavelength $\lambda_B$ (nm) | FBG number | Wavelength $\lambda_B$ (nm) |
|---|-----------------------------|------------|-----------------------------|
| 1   | 1529.0855                   | 5          | 1550.383                    |
| 2   | 1532.9348                   | 6          | 1554.3619                   |
| 3   | 1538.6864                   | 7          | 1559.5727                   |
| 4   | 1544.6879                   | 8          | 1562.8105                   |
| Temperature of subgrade 25 cm below the subgrade surface (°C) |                             | 23.2       |                             |
| Temperature of subgrade 50 cm below the subgrade surface (°C) |                             | 22.9       |                             |

where  $EI$  is the bending stiffness. This can be rewritten as follows:

$$\Delta B = \int_0^l \frac{M(x)\overline{M(x)}}{EI} dx + \int_0^l \frac{M_1(x)\overline{M(x)}}{EI} dx + \int_0^l \frac{M_2(x)\overline{M(x)}}{EI} dx, \quad (17)$$

where the terms  $M(x)$ ,  $M_1(x)$ , and  $M_2(x)$  are the bending moments of the cantilever beam under an external load ( $F, q_1, q_2$ ), which are defined as follows:

$$M(x) = \frac{\varepsilon(x)EI}{y}. \quad (18)$$

Here, the horizontal strain  $\varepsilon$  is now a function of  $x$ , and  $y$  is the distance from a point on the monitoring tube along the radial direction to the beam centerline axis.

The analysis at point  $B$  is now extended to some arbitrary point  $C$  along the horizontal direction of the cantilever beam of radius  $R$ , as shown in Figure 16. Here, the bending moment equation under  $f$  is given as

$$\overline{M}(x) = -x. \quad (19)$$

The relationship between the vertical displacement and the horizontal strain at point  $C$  is given as follows:

$$\Delta C = \int_0^x \frac{M(x)\overline{M}(x)}{EI} dx = \int_0^x \frac{\varepsilon(x)}{y} \cdot (-x) dx. \quad (20)$$

The horizontal strain can be analyzed more clearly by considering a short segment of the cantilever beam of length  $dx$  at  $C$  in Figure 16 and expanding it as illustrated in Figure 17(a), where  $y$  is the distance between any longitudinal line segment  $MM'$  and the centerline axis  $OO'$ . This is applied to a case of pure beam bending through an arc of  $d$ , as illustrated in Figure 17(b), where the strain is given as

$$\varepsilon(x) = \frac{(\rho + y)d\theta - \rho d\theta}{\rho d\theta} = \frac{y}{\rho}, \quad (21)$$

and  $\rho$  is the radius of curvature of the centerline axis after bending. According to formulas (20) and (21), the deflection of point  $C$  under stress can be obtained as follows:

$$\Delta C = -\frac{x^2}{2\rho}, \quad (22)$$

which represents the collaborative deformation of the monitoring tube and soil under an applied force. Here, the minus sign ( $-$ ) indicates that the deflection is downward, and the value of  $\rho$  can be determined from experimental measurement data.

TABLE 6: Center wavelengths of the reflected light from the FBGs obtained immediately after completion of the test roadway pavement layer.

| FBG number | Wavelength $\lambda_B$ (nm) | FBG number | Wavelength $\lambda_B$ (nm) |
|------------|-----------------------------|------------|-----------------------------|
| 1          | 1528.7945                   | 5          | 1550.1154                   |
| 2          | 1532.2087                   | 6          | 1553.687                    |
| 3          | 1538.3975                   | 7          | 1559.3029                   |
| 4          | 1543.9701                   | 8          | 1562.1249                   |

TABLE 7: Subgrade deformation and temperature during construction.

| Test point                                  | Position ① | Position ② | Position ③ | Position ④ |
|---|------------|------------|------------|------------|
| Vertical deformation of subgrade (mm)       | 12.9       | 15.4       | 11.9       | 14.8       |
| Subgrade temperature ( $^{\circ}\text{C}$ ) | 11.6       | 11.8       | 11.3       | 11.2       |

TABLE 8: Center wavelengths of the reflected light from the FBGs before conducting vehicle load testing.

| FBG number | Wavelength $\lambda_B$ (nm) | FBG number | Wavelength $\lambda_B$ (nm) |
|------------|-----------------------------|------------|-----------------------------|
| 1          | 1529.1708                   | 5          | 1550.4245                   |
| 2          | 1532.2865                   | 6          | 1553.7409                   |
| 3          | 1538.7567                   | 7          | 1559.6177                   |
| 4          | 1544.0419                   | 8          | 1562.1852                   |

## 5. On-Site Monitoring of Subgrade Deformation

**5.1. Monitoring Tube Installation under Test Roadway.** The monitoring tubes were packaged according to the design in Figure 5 and installed in the subgrade soil underneath a test roadway section according to the layout scheme illustrated in Figure 7. The embedding process is shown in Figure 18.

**5.2. Initial Data Acquisition.** The initial center wavelength of the reflected light from the 8 FBGs and the temperature of the subgrade was collected immediately after laying the two monitoring tubes. The test data were collected using a sm130 FBG demodulator (American Micron Optics, Inc.). The sm130 demodulator includes a built-in large-bandwidth scanning laser light source. It also includes 4 channels with a wavelength range of 1510–1590 nm and an accuracy higher than 1 pm. Bluetooth wireless temperature measurement devices with low power consumption were embedded in the subgrade at depths corresponding to the monitoring tubes [49]. The collected data are listed in Table 5. The FBG monitoring system requires only the initial temperature from the wireless temperature sensors, and subsequent subgrade temperatures can be obtained by monitoring the change in the  $\lambda_B$  values of the respective FBGs.

TABLE 9: Total deformation and temperature of the subgrade during summer.

| Test point                            | Position ① | Position ② | Position ③ | Position ④ |
|---------------------------------------|------------|------------|------------|------------|
| Vertical deformation of subgrade (mm) | 8.9        | 10.4       | 7.5        | 9.1        |
| Subgrade temperature (°C)             | 16.8       | 16.7       | 16.4       | 16.4       |

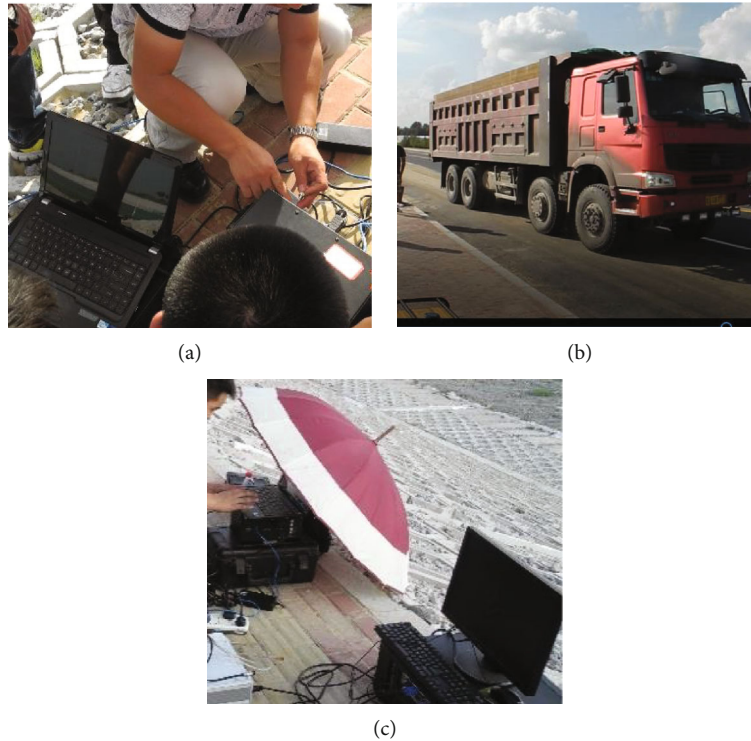


FIGURE 19: Vehicle load strain monitoring site of the test roadway: (a) FBGs connected with the acquisition equipment; (b) vehicle passing the monitoring section; (c) data acquisition.

According to formula (11), the wavelength changes of FBG1 and FBG2 monitoring tube 1 in Figure 7 are as follows:

$$\begin{aligned}\Delta\lambda_{B1} &= K_\varepsilon\varepsilon_1 + K_T\Delta T_1, \\ \Delta\lambda_{B2} &= K_\varepsilon\varepsilon_2 + K_T\Delta T_2,\end{aligned}\quad (23)$$

where  $\Delta T_1$  and  $\Delta T_2$  are the subgrade temperature difference between the monitoring time and the initial time.  $\Delta\lambda_{B1}$  and  $\Delta\lambda_{B2}$  can be obtained by monitoring. It can be seen from Figure 17 that  $\varepsilon_1 = -\varepsilon_2$ . Since the subgrade temperature change is small within 10 cm,  $\Delta T_1 = \Delta T_2$  can be set. The strain and temperature changes of FBG1 and FBG2 are calculated as follows:

$$\begin{aligned}\varepsilon_1 = -\varepsilon_2 &= \frac{\Delta\lambda_{B1} - \Delta\lambda_{B2}}{2K_\varepsilon}, \\ \Delta T_1 = \Delta T_2 &= \frac{\Delta\lambda_{B1} + \Delta\lambda_{B2}}{2K_T}.\end{aligned}\quad (24)$$

Therefore, as long as the initial temperature of the monitoring point is known, the subgrade temperature at

point ① in Figure 7 can be calculated when monitoring. According to the method, the temperature of points ②, ③, and ④ in Figure 7 can also be calculated.

Similarly, the center values of  $\lambda_B$  obtained from the 8 FBGs were collected immediately after the pavement of the test roadway was completed. The collected data are listed in Table 6. Finally, the deformation of the subgrade at the monitoring points during the construction period was calculated based on the data collected before and after construction, and the subgrade temperature at the completion of roadway paving was also obtained. These results are listed in Table 7 along with vertical deformation and temperatures of the subgrade obtained after construction.

**5.3. Subgrade Deformation Monitoring under Vehicle Loading.** Subgrade deformation monitoring of the test roadway under vehicle loading was conducted during the summer of the second year after the roadway was opened to traffic. First, the center wavelengths of the reflected light from the FBGs were collected, and the collection results are listed in Table 8. The permanent deformation of the subgrade at the monitoring points since the completion of the roadway

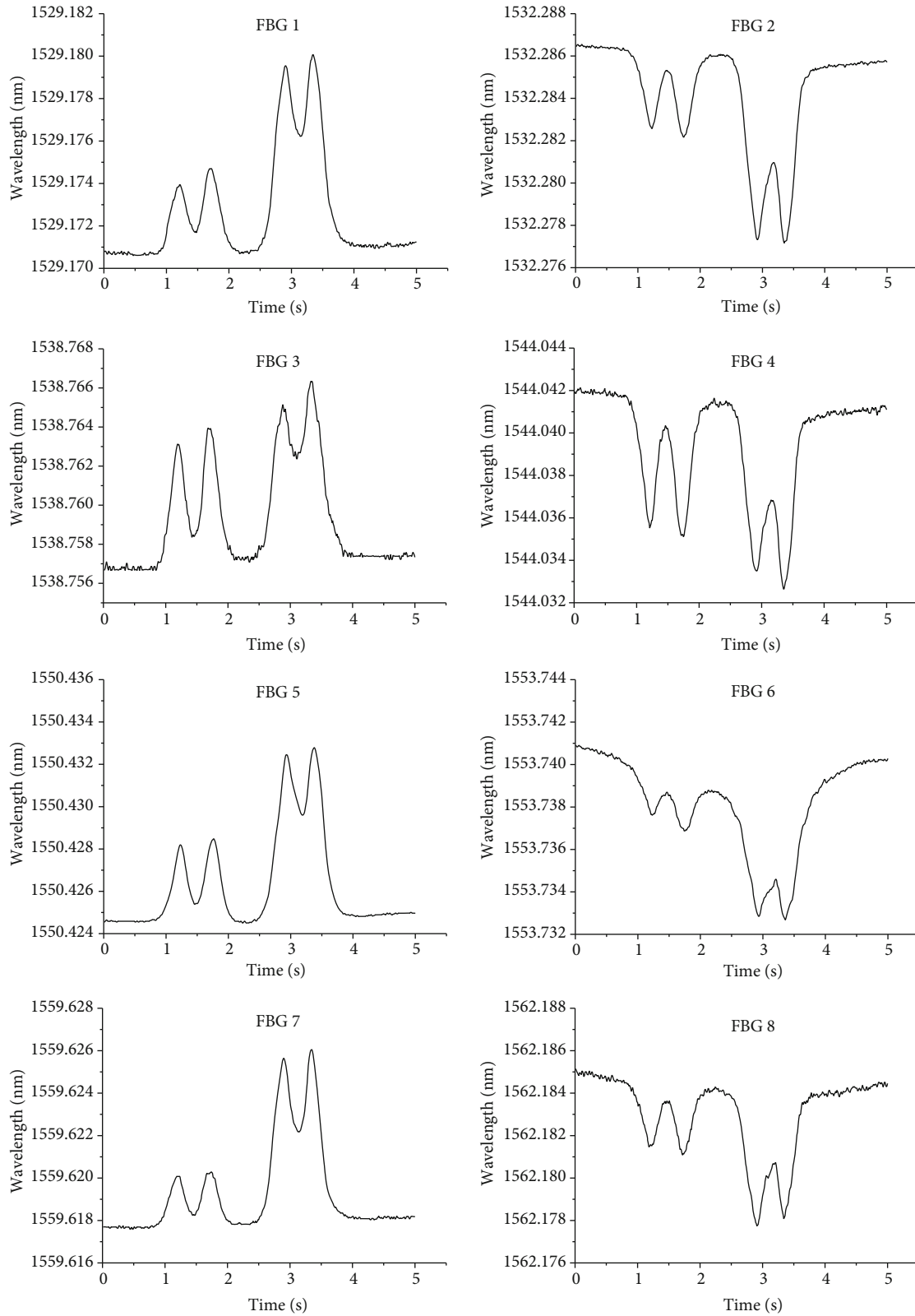


FIGURE 20: Time histories of the values of  $\lambda_B$  obtained for the 8 FBGs under vehicle loading

surface was then calculated based on the data collected in Tables 6 and 8, and the results are listed in Table 9 along with the calculated subgrade temperature at the time of monitoring.

We conducted dynamic subgrade deformation monitoring under vehicle loading using a heavy 4-axle truck traveling over the subgrade monitoring area at a speed of 10 km/h. The dynamic load monitoring test process is shown in Figure 19.

TABLE 10: Subgrade deformation determined under vehicle loading.

| Deformation   | Position ① | Position ② | Position ③ | Position ④ |
|---|------------|------------|------------|------------|
| Maximum deformation under dynamic loading ( $\mu\text{m}$ ) | 556.32     | 695.40     | 485.58     | 574.02     |
| Elastic deformation ( $\mu\text{m}$ )                       | 515.37     | 642.39     | 451.37     | 532.48     |
| Permanent deformation ( $\mu\text{m}$ )                     | 40.96      | 53.00      | 34.22      | 41.54      |

The time histories of the values of  $\lambda_B$  obtained for the 8 FBGs under vehicle loading are presented in Figure 20. The maximum deformation, elastic deformation, and permanent deformation of each monitoring point under vehicle loading were determined from the collected data, and the results are listed in Table 10.

It can be seen from Figure 20 that the FBG monitoring system accurately monitors the process by which the values of  $\lambda_B$  change with respect to time under dynamic vehicle loading conditions, and the monitoring system can effectively detect the maximum deformation, elastic deformation, and permanent deformation of the subgrade from the time histories. It can be seen from Table 10 that the deformation values obtained by the FBGs increase as the distance between the FBGs on the cantilever beam and the anchor point in the concrete column increases. We then selected the larger value as the monitoring result. We also note that the maximum deformation, elastic deformation, and permanent deformation values of the subgrade decrease substantially with increasing distance from the subgrade surface.

The subgrade deformation was obtained by analyzing the data collected by the monitoring tube 1 and tube 2 under the load of vehicles such as a light vehicle, water truck, medium truck, transit mixer truck, and heavy truck during the fall of the second year after the roadway was opened to traffic. These results are shown in Figure 21. The subgrade deformation value was randomly monitored during the normal driving process of the vehicles; also, it was affected by many factors such as vehicle speed and cargo load.

It can be seen from Figure 21 that the deformation law of subgrade obtained by the two monitoring pipes under different loads is the same. The permanent deformation values of deep subgrade are smaller than those of shallow subgrade. It indicates that the permanent deformation of the subgrade decreases with the increase of the subgrade depth under the action of load. The permanent deformation of the subgrade is very little under the action of a light truck, but it increases obviously when the load increases. The order of magnitude and variation law of the subgrade deformation obtained by the monitoring method are similar to those obtained in the literatures [46, 50].

## 6. Conclusions

The present work addressed the difficulty of monitoring the deformation of highway subgrades in situ using FBG sensing technology. An FBG was encapsulated within a monitoring tube formed from a PVC tube, and one end of the monitoring tube was fixed perpendicular to a concrete column, forming a cantilever beam monitoring sys-

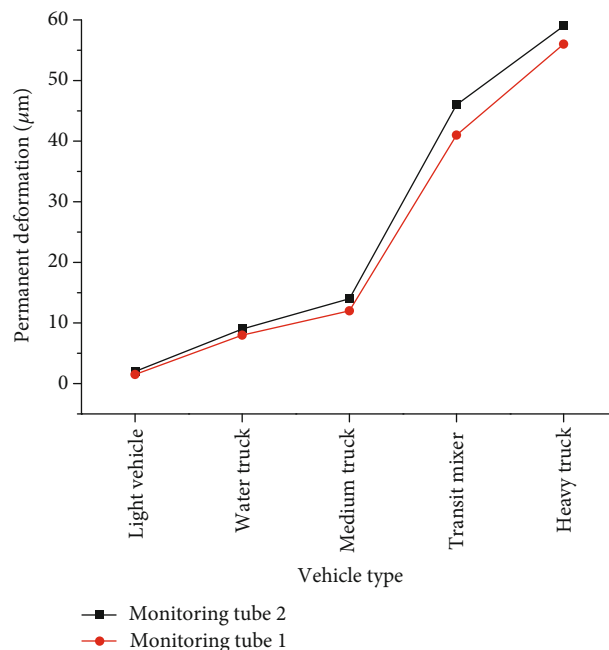


FIGURE 21: Subgrade deformation under different loads

tem. The deformation was assessed according to the theoretical relationship between the horizontal strain on the FBG embedded in the monitoring tube and the vertical displacement of the cantilever beam. Then, the relationship between the variation in the wavelength of light reflected by the encapsulated FBG and the temperature and horizontal strain was obtained on this basis by calibration experiments. Two monitoring tubes were buried at depths of 25 cm and 50 cm below the subgrade surface of a test roadway, and the system was demonstrated to facilitate the monitoring of the deformation and temperature of the subgrade at different stages of construction through the collection of FBG wavelength data during different periods, which included after embedding the monitoring tubes, after the completion of the test roadway surface, and during a period of operation under dynamic vehicle loading. The proposed monitoring system was verified to effectively detect the maximum deformation, elastic deformation, and permanent deformation of the subgrade from the time histories of the center wavelengths of the light reflected by the FBGs under conditions of dynamic loading. Accordingly, we can conclude that the FBG monitoring system can realize long-term, accurate, and efficient monitoring of subgrade deformation as well as subgrade temperature in the range of  $-20^{\circ}\text{C}$  to  $30^{\circ}\text{C}$ .

## Data Availability

The data used to support the findings of this study are available from the corresponding author upon request.

## Conflicts of Interest

The authors declare that they have no conflicts of interest.

## References

- [1] Y.-c. Cheng and Z.-w. Shi, "Experimental study on Nano-SiO<sub>2</sub> improving concrete durability of bridge deck pavement in cold regions," *Advances in Civil Engineering*, vol. 2019, 9 pages, 2019.
- [2] A. J. Puppala and C. S. Chittoori, "Transportation infrastructure settlement and heave distress: challenges and solutions," *Journal of Zhejiang University Science A*, vol. 13, no. 11, pp. 850–857, 2012.
- [3] X. Xing, L. Chen, Z. Yuan, and Z. Shi, "An improved time-series model considering rheological parameters for surface deformation monitoring of soft clay subgrade," *Sensors*, vol. 19, no. 14, p. 3073, 2019.
- [4] G. Wang, X. Wei, and J. Zhao, "Modelling spiky acceleration response of dilative sand deposits during earthquakes with emphasis on large post-liquefaction deformation," *Earthquake Engineering and Engineering Vibration*, vol. 17, no. 1, pp. 125–138, 2018.
- [5] J. Yang, *Study on Method and System for Automatically Measuring and Monitoring Multi-Parameters of Subgrade Settlement*, Beijing Jiaotong University, Beijing, China, 2014.
- [6] Y.-h. Shi, "Monitoring analysis of subgrade settlement of expressway high-fill subgrade," *Western China Communications Science & Technology*, vol. 4, pp. 73–76, 2019.
- [7] M. Wang, S.-j. Meng, Y.-q. Sun, and H. Fu, "Shear strength of frozen clay under freezing-thawing cycles using triaxial tests," *Earthquake Engineering and Engineering Vibration*, vol. 17, no. 4, pp. 761–769, 2018.
- [8] J.-y. Xu, J. X. Li, J. Yang, Y. Gao, and S. Wu, "A remote subgrade settlement monitoring system based on optical method," *Urban Rail Transit*, vol. 5, no. 3, pp. 202–206, 2019.
- [9] K. O. Hill, Y. Fujii, D. C. Johnson, and B. S. Kawasaki, "Photosensitivity in optical fiber waveguides: application to reflection filter fabrication," *Applied Physics Letters*, vol. 32, no. 10, pp. 647–649, 1978.
- [10] G. Meltz, W. W. Morey, and W. H. Glenn, "Formation of Bragg gratings in optical fibers by a transverse holographic method," *Optics Letters*, vol. 14, no. 15, pp. 823–825, 1989.
- [11] P. Ferreira, E. Caetano, L. Ramos, and P. Pinto, "Shape sensing monitoring system based on fiber-optic strain measurements: laboratory tests," *Experimental Techniques*, vol. 41, no. 4, pp. 407–420, 2017.
- [12] Y. Kuang, Y.-x. Guo, L. Xiong, and W. Liu, "Packaging and temperature compensation of fiber Bragg grating for strain sensing: a survey," *Photonic Sensors*, vol. 8, no. 4, pp. 320–331, 2018.
- [13] F.-g. Su, *Investigation on Applications of Fiber Bragg Grating in Sensing Technology*, Beijing University of Posts and Telecommunications, Beijing, China, 2013.
- [14] G.-q. Xu and D.-y. Xiong, "Applications of fiber Bragg grating sensing technology in engineering," *Chinese Optics*, vol. 6, no. 3, pp. 306–317, 2013.
- [15] G. Kaklauskas, A. Sokolov, R. Ramanauskas, and R. Jakubovskis, "Reinforcement strains in reinforced concrete tensile members recorded by strain gauges and FBG sensors: experimental and numerical analysis," *Sensors*, vol. 19, no. 1, p. 200, 2019.
- [16] H.-b. Xu, F. Li, W.-g. Zhao, S. Wang, Y. du, and C. Bian, "A high precision fiber Bragg grating inclination sensor for slope monitoring," *Journal of Sensors*, vol. 2019, Article ID 1354029, 7 pages, 2019.
- [17] Y. Li, H.-p. Wang, W.-s. Zhu, S. Li, and J. Liu, "Structural stability monitoring of a physical model test on an underground cavern group during deep excavations using FBG sensors," *Sensors*, vol. 15, no. 9, pp. 21696–21709, 2015.
- [18] H.-k. Gong, M. S. Kizil, Z.-w. Chen, M. Amanzadeh, B. Yang, and S. M. Aminossadati, "Advances in fibre optic based geotechnical monitoring systems for underground excavations," *International Journal of Mining Science and Technology*, vol. 29, no. 2, pp. 229–238, 2019.
- [19] D.-d. Cao, H.-y. Fang, F.-m. Wang, H. Zhu, and M. Sun, "A fiber Bragg-grating-based miniature sensor for the fast detection of soil moisture profiles in highway slopes and subgrades," *Sensors*, vol. 18, no. 12, p. 4431, 2018.
- [20] Z.-f. Wang, *Study on Fiber Bragg Grating Sensing Theory and Key Technology for Bridges and Tunnels Engineering Safety Monitoring*, Shandong University, Jinan, China, 2014.
- [21] Z. Zhou and Z.-z. Wang, "An experimental investigation on flexural behavior of reinforced concrete beams strengthened by an intelligent CFRP plate with built-in optical fiber Bragg grating sensors," *Journal of Sensors*, vol. 2018, 16 pages, 2018.
- [22] S.-g. Deng, X. Ma, and X.-w. Li, "The analysis of angle resolution of stress vector sensor based on optical fiber sensing cable for high speed railway traffic," *Journal of Shanghai Jiaotong University (Science)*, vol. 23, no. 1, pp. 61–65, 2018.
- [23] S.-q. Sun, S.-c. Li, L.-p. Li, S. S. Shi, Z. Q. Zhou, and C. L. Gao, "Design of a displacement monitoring system based on optical grating and numerical verification in geomechanical model test of water leakage of tunnel," *Geotechnical and Geological Engineering*, vol. 36, no. 4, pp. 2097–2108, 2018.
- [24] H.-t. Zhao, Q.-b. Wang, Y. Qiu, J. A. Chen, Y. Y. Wang, and Z. M. Fan, "Sstrain transfer of surface-bonded fiber Bragg grating sensors for airship envelope structural health monitoring," *Journal of Zhejiang University Science A*, vol. 13, no. 7, pp. 538–545, 2012.
- [25] C. S. Shin, B. L. Chen, and S. K. Liaw, "An FBG-based impact event detection system for structural health monitoring," *Advances in Civil Engineering*, vol. 2010, Article ID 253274, 8 pages, 2010.
- [26] J. Johnny, R. Prabhu, and W. K. Fung, "Investigation of structural parameter dependence of confinement losses in PCF-FBG sensor for oil and gas sensing applications," *Optical and Quantum Electronics*, vol. 48, no. 4, 2016.
- [27] C.-d. Piao, D. Wang, H. Kang, H. He, C. Zhao, and W. Liu, "Model test study on overburden settlement law in coal seam backfill mining based on fiber Bragg grating technology," *Arabian Journal of Geosciences*, vol. 12, no. 13, article 4564, pp. 1–9, 2019.
- [28] Y.-x. Guo, D.-s. Zhang, Z.-d. Zhou et al., "A novel surface-mounted FBG strain sensor and its application in highway bridge engineering," *Journal of Optoelectronics Laser*, vol. 25, no. 3, pp. 435–441, 2014.
- [29] K. Kesavan, K. Ravikiran, R. Senthil, B. Arun Sundaram, and S. Parivallal, "FBG sensor technology to interfacial strain

- measurement in CFRP-strengthened concrete beam,” *Experimental Techniques*, vol. 39, no. 5, pp. 21–29, 2015.
- [30] L. Alwis, H. Bustamante, B. Roth, K. Bremer, T. Sun, and K. T. V. Grattan, “Evaluation of the durability and performance of FBG-based sensors for monitoring moisture in an aggressive gaseous waste sewer environment,” *Journal of Lightwave Technology*, vol. 35, no. 16, pp. 3380–3386, 2017.
- [31] B. Torres Górriz, P. Rinaudo, and P. A. Calderón García, “Comparison between point and long-gage FBG-based strain sensors during a railway bridge load test,” *Strain*, vol. 53, no. 4, article e12230, 2017.
- [32] U. Nawrot, T. Geernaert, B. De Pauw et al., “Mechanical strain-amplifying transducer for fiber Bragg grating sensors with applications in structural health monitoring,” in *25th International Conference on Optical Fiber Sensors*, April 2017, Jeju, Korea.
- [33] A. V. Dyshlyuk, N. V. Makarova, and O. B. Vitrik, “Strain monitoring of reinforced concrete with OTDR-based FBG interrogation technique,” *Smart Structures and Systems*, vol. 20, no. 3, pp. 343–350, 2017.
- [34] G.-n. Wang, D.-k. Liang, and J.-f. Yan, “A vibration-based method for the measurement of subgrade soil scaling factor,” *Photonic Sensors*, vol. 8, no. 4, pp. 375–383, 2018.
- [35] M. Bellas and G. Voulgaridis, “Study of the major landslide at the community of Ropoto, Central Greece, mitigation and FBG early warning system design,” *Innovative Infrastructure Solutions*, vol. 3, no. 1, p. 30, 2018.
- [36] Q.-m. Nan, S. Li, Y.-q. Yao et al., “A novel monitoring approach for train tracking and incursion detection in underground structures based on ultra-weak FBG sensing array,” *Sensors*, vol. 19, no. 12, p. 2666, 2019.
- [37] Y.-k. Cheng, S.-j. Meng, Y.-l. Wang, L. Lin, and S.-r. Zhang, “Application of fiber Bragg grating in monitoring subgrade deformation under dynamic load,” *Chinese Journal of Underground Space and Engineering*, vol. 10, no. S2, pp. 1887–1892, 2014.
- [38] S.-j. Meng, S.-r. Zhang, Y.-k. Cheng, W. Yun-long, W. Yu, and S. Yi-qiang, “Application of fiber Bragg grating sensors to strain detection of seasonally frozen subgrade,” *Rock Soil Mechanics*, vol. 37, no. 2, pp. 601–608, 2016.
- [39] H. Zhang, B. Xu, and Y.-p. Liu, *Theory and Practice of FBG Monitoring in Geotechnical Engineering*, China Architecture & Building Press, Beijing, China, 2018.
- [40] Z.-x. Wu and F. Wu, *Principle and Application of FBG Sensor*, National Defense Industry Press, Beijing, China, 2011.
- [41] L. Zhang, B. Shi, L. Zeni, A. Minardo, H. Zhu, and L. Jia, “An fiber Bragg grating-based monitoring system for slope deformation studies in geotechnical centrifuges,” *Sensors*, vol. 19, no. 7, p. 1591, 2019.
- [42] R. He, W.-f. Wu, H.-x. Chen, and X. Huang, “Research progress on fiber Bragg grating sensors in road testing and engineering,” *Bulletin of the Chinese Ceramic Society*, vol. 36, no. 6, pp. 1912–1919, 2017.
- [43] Y. Chen and H.-l. Liu, *Fiber Grating Sensing Technology and Application*, Science Press, Beijing, China, 2018.
- [44] D.-d. Pang, *Investigation on the Novel Fiber Bragg Grating Sensing Technology*, Shandong University, Jinan, China, 2014.
- [45] J. Wang, J.-s. Zang, F. Meng, and L. Song, “Study on dynamic response of highway subgrade under traffic loads,” *Subgrade Engineering*, vol. 2, pp. 7–10, 2013.
- [46] S.-j. Meng, Y.-q. Sun, and M. Wang, “Fiber Bragg grating sensors for subgrade deformation monitoring in seasonally frozen regions,” *Structural Control and Health Monitoring*, vol. 27, no. 1, 2019.
- [47] C. Yang, Z.-y. Li, and C. Dong, “Study on the method of determine roadbed work area based on the dynamic stress,” *Highway Engineering*, vol. 39, no. 2, pp. 115–118, 2014.
- [48] Z. Lu, C. B. Wang, J. J. Fu, and Y. X. Zhan, “Research on influence depth of road subgrade induced by vehicle loads,” *Rock Soil Mechanics*, vol. 34, no. 2, pp. 316–321, 2013.
- [49] Y. Wang, S.-j. Meng, J.-h. Yuan, S.-r. Zhang, Y. Gao, and D.-w. Pang, “Application of Bluetooth low energy for roadbed temperature test in seasonal frozen area,” *Journal of Harbin University of Science and Technology*, vol. 21, no. 5, pp. 40–44, 2016.
- [50] F. Zhang, B. Lin, D.-c. Feng, and X. Z. Ling, “Permanent deformation of subgrade induced by long-term truck traffic loading,” *Journal of Harbin Institute of Technology*, vol. 49, no. 3, pp. 120–126, 2017.